PAPER

One-dimensional weak antilocalization effect in 1T′-MoTe$_2$ nanowires grown by chemical vapor deposition

View the article online for updates and enhancements.

IOP ebooks™

Bringing together innovative digital publishing with leading authors from the global scientific community.

Start exploring the collection–download the first chapter of every title for free.

One-dimensional weak antilocalization effect in 1T′-MoTe₂ nanowires grown by chemical vapor deposition

Jiancui Chen[1,2] , **Zhang Zhou**[1,2], **Hongtao Liu**[1,2], **Ce Bian**[1,2], **Yuting Zou**[1,2], **Zhenyu Wang**[1,2], **Zhen Zhao**[1,2], **Kang Wu**[1,2], **Haitao Yang**[1,2,3], **Chengmin Shen**[1,2,3], **Zhi Gang Cheng**[1,2], **Lihong Bao**[1,2,3,∗] and **Hong-Jun Gao**[1,2,3]

[1] Institute of Physics, Chinese Academy of Sciences, PO Box 603, Beijing 100190, People's Republic of China
[2] University of Chinese Academy of Sciences and CAS Center for Excellence in Topological Quantum Computation, Chinese Academy of Sciences, PO Box 603, Beijing 100190, People's Republic of China
[3] Songshan Lake Materials Laboratory, Dongguan 523808, Guangdong, People's Republic of China

E-mail: lhbao@iphy.ac.cn

CrossMark

Abstract

We present a chemical vapor deposition method for the synthesizing of single-crystal 1T′-MoTe₂ nanowires and the observation of one-dimensional weak antilocalization effect in 1T′-MoTe₂ nanowires for the first time. The diameters of the 1T′-MoTe₂ nanowires can be controlled by changing the flux of H_2/Ar carrier gas. Spherical-aberration-corrected transmission electron microscopy, selected area electron diffraction and energy dispersive x-ray spectroscopy (EDS) reveal the 1T′ phase and the atomic ratio of Te/Mo closing to 2:1. The resistivity of 1T′-MoTe₂ nanowires shows metallic behavior and agrees well with the Fermi liquid theory (<20 K). The coherence length extracted from 1D Hikami–Larkin–Nagaoka model with the presence of strong spin–orbit coupling is proportional to $T^{-0.36}$, indicating a Nyquist electron–electron interaction dephasing mechanism at one dimension. These results provide a feasible way to prepare one-dimensional topological materials and is promising for fundamental study of the transport properties.

Keywords: chemical vapor deposition, 1T′-MoTe₂ nanowire, spin–orbit coupling, one-dimensional weak antilocalization effect

S Supplementary material for this article is available online

(Some figures may appear in colour only in the online journal)

1. Introduction

In past few years, TMDCs are rising as an emerging class of quantum materials after witnessed the discovery of their novel topological properties beyond the electronic applications [1, 2], such as Weyl semimetal [3], Dirac semimetal [4], node line [5], and topological insulator [6–8] etc. The broad spectrum of the properties of the TMDCs is coming from the diversity of their compositions and structures, including trigonal prismatic (2H), octahedral (1T), and monoclinic (1T′) phases etc [9]. As a typical member of the TMDCs family, MoTe₂ possesses three structural phases, including semiconducting 2H, metallic T_d, and semi-metallic 1T′ phases [10]. The reversible structural phase transition between the 2H and 1T′ phases can be induced through the Peierls distortion by tuning the propor-

∗ Author to whom any correspondence should be addressed.

tion of ingredients during CVD growth [11–13] or by applying mechanical strain using an atomic force microscope (AFM) tip. [14] In the band structure of the 1T′-MoTe$_2$, the positions of the valence and conduction band edges change with reduced thickness, which gives rise to their distinct thickness-dependent properties. For 1T′-MoTe$_2$ bulk crystal, the type-II Weyl semimetal nature has been confirmed by observation of the topological Fermi arcs using angle-resolved photoemission spectroscopy [15], and the planar hall effect caused by the chiral anomaly has also been discovered [16]. When reduced its thickness to a few layers, 1T′-MoTe$_2$ exhibits a bandgap opening of up to 60 meV arising from strong spin–orbit coupling (SOC) [11]. Further reducing its thickness to the monolayer limit, spontaneous symmetry breaking is occurred due to the relative atomic displacements of Mo atoms and Te atoms, and robust room-temperature out-of-plane ferroelectricity has been observed [17]. The nature of quantum spin Hall insulators in the monolayer 1T′-MoTe$_2$ has also been predicted, which results from an intrinsic band inversion between chalcogen-p and metal-d bands for the structural distortion based on non-trivial Z_2-band-topology [18].

Stacking distortion will happen in the 1T′-MoTe$_2$ when the inversion symmetry was broken with the change of the dimension or the temperature. In bulk MoTe$_2$, the structural transition from centrosymmetric monoclinic 1T′ phase to noncentrosymmetric orthorhombic T$_d$ phase under 250 K results in a hysteresis in the temperature-dependent resistivity, while in the few-layered MoTe$_2$, only T_d phase exists under 300 K [19]. Therefore, at the room temperature, the MoTe$_2$ crystallizes in 1T′ phase in 3D and $1T_d$ phase in 2D. Except the phase transition, the magnetoresistance (MR) is gradually suppressed due to the decrease of the carrier mobility and increase of the electron–hole imbalance with reduced thickness [20], suggesting that the transport properties of 1T′-MoTe$_2$ is strongly dependent on its dimensions. However, the transport properties of one-dimensional 1T′-MoTe$_2$ still remain elusive.

In this work, we have successfully prepared high-quality 1T′-MoTe$_2$ nanowires with tunable diameters from ∼80 to ∼27 nm by chemical vapor deposition method. The 1T′-MoTe$_2$ nanowires can also be epitaxially grown on mica (001) along three directions with an angle of 60° between each other. The chemical composition and crystallographic structure of 1T′-MoTe$_2$ nanowires is confirmed by AC-HRTEM, selected area electron diffraction (SAED), EDS and Raman spectroscopy. The temperature-dependent resistivity of as-grown 1T′-MoTe$_2$ nanowires shows metallic behavior. Weak antilocalization (WAL) effect in as-grown 1T′-MoTe$_2$ nanowires is evidenced by the appearance of the cusp at around zero magnetic fields in the MR with temperatures up to ∼3 K. Analyzing the WAL effect by 1D HLN equation with strong SOC, the temperature-dependent phase coherence length L_ϕ can be extracted. The phase coherence length L_ϕ shows a power law dependence with temperature, $L_\phi \sim T^{-0.36}$, revealing a clear quasi-one-dimensional transport nature and Nyquist electron–electron interaction dephasing mechanism. The two-dimensional WAL effect has been found in the few-layered 1T′-MoTe$_2$ nanosheets in previous study [21]. The existence

of the one-dimensional WAL effect in 1T′-MoTe$_2$ nanowires proves that the WAL effect would not vanish even when lowering the dimension from two to one, indicating the robust WAL effect arises from strong SOC. These results provide a pathway to prepare the high quality 1T′-MoTe$_2$ nanowires and set a stage for further exploration of 1D 1T′-MoTe$_2$ along with its application in the future quantum devices.

2. Experiments

2.1. Synthesis of the 1T′-MoTe$_2$ nanowire

1T′-MoTe$_2$ nanowires were grown by two-step chemical vapor deposition method using tellurium blocks and MoO$_3$ single crystal as precursors in a three-zone tube furnace. The high-quality MoO$_3$ single crystal as the precursor was grown onto a mica substrate by directly oxidizing Mo foil in air at 600 °C for 20 min in a one-zone tube furnace. The obtained MoO$_3$ single crystal on mica was placed on SiO$_2$ (280 nm)/Si substrate in a quartz tube in which tellurium (⩾99.999%, 9 g, alfa) blocks are placed upstream. In a typical growth process, firstly, the furnace was evacuated to 10^{-2} torr and high-purity Ar was introduced at 100 sccm for 20 min to eliminate residual oxygen. Then, the MoO$_3$@ SiO$_2$/Si substrate was heated up to 580 °C and the upstream tellurium blocks were heated up to 680 °C for 15 min under a mixture of argon and hydrogen carrier gas at a flow rate of 100 sccm (standard cubic centimeters per minute) (Ar:H$_2$ = 10:1). After that, the furnace was cooled down to room temperature naturally.

2.2. Characterization

The morphology of the as-grown MoTe$_2$ nanowires was characterized by optical microscope (Olympus BX51-SC30). The diameter of the nanowires was determined by an AFM (digital instruments nanoscope IIIa and dimension edge, Bruker) operated in tapping mode. Raman spectrum was conducted on samples directly after growth and performed under ambient conditions with an excitation wavelength of 532 nm using a customized Raman spectrometer (WITec alpha 300R). For aberration-corrected transmission electron microscopy (ACTEM) imaging of MoTe$_2$ nanowire, the material was transferred onto a holey-carbon TEM grid using a water-soluble polymer mediator. Firstly, 0.75 g of polyvinylpyrrolidone (PVP) (Alfa Aesar, average MW 58 000), 1.5 ml of N-vinylpyrrolidone (NVP) (aladdin, 99%), and 0.75 ml of H$_2$O were dissolved in ethanol to prepare 10 ml of solution. A drop of this solution was spin-coated on the SiO$_2$/Si substrate with MoTe$_2$ nanowires at 800 rpm for 1 min, followed by removing the solvents in air without baking. After that, 10 wt % poly (vinyl alcohol) (alfa, 86%–89% hydrolyzed, medium molecular weight) aqueous solution was spin-coated on the top of PVP film followed by removing the solvents in air without baking. Then, the polymer mediator carrying MoTe$_2$ nanowires were scratched and peeled by a blade at the edges of the substrate. Next, the polymer mediator was attached to the target holey-carbon TEM grid on the glasses. For the close contact between material and the grid, a drop of the ethanol was added on the
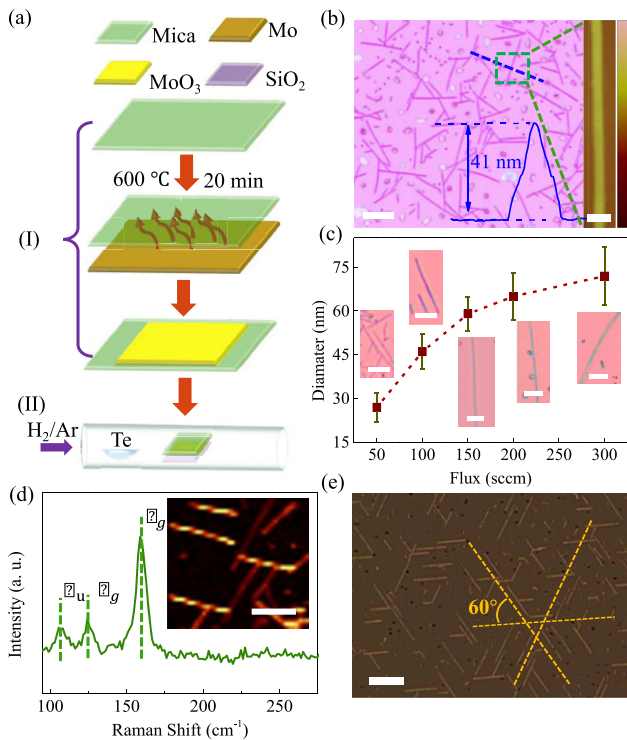
Figure 1. Preparation and characterization of 1T′-MoTe₂ nanowires. (a) Schematic illustration of the CVD growth process of MoTe₂ nanowires. (b) Typical optical image of as-grown MoTe₂ nanowires on a 280 nm SiO₂/Si substrate under 580 °C and 100 sccm Ar/H₂ flow. Scale bar: 10 μm. Right inset: AFM topographic image of MoTe₂ nanowire. Scale bar: 100 nm. The height profile (blue curve) indicates the diameter of the MoTe₂ nanowire scanned by the blue dash line is 41 nm. (c) The average diameter of MoTe₂ nanowires as a function of different gas-flux at 580 °C. Insets: optical images of MoTe₂ nanowires with different diameters on 280 nm SiO₂/Si. Scale bars: 3 μm. (d) Raman spectrum of the MoTe₂ nanowires. Three prominent peaks at 105, 127, 161 cm^{-1} corresponding to A$_u$, A$_g$ and B$_g$ modes in 1T′-MoTe₂, respectively. Inset: Raman mapping of the amplitude of the 161 cm^{-1} peak. Scale bar: 5 μm. (e) The optical image of MoTe₂ nanowires grown on mica substrate under 580 °C and 100 sccm Ar/H₂ flow. A 60° angle between nanowires highlighted by yellow dashed line, suggesting an epitaxial mechanism. Scale bar: 10 μm.

Figure 2. Micro-structural characterization of the 1T′-MoTe₂ nanowire. (a) Transmission electron microscopy (TEM) image of an individual nanowire. Scale bar: 50 nm. (b) SAED pattern of the nanowire shown in (a), which is viewed from zone axis [0 0 −2]. Scale bar: 5 nm^{-1}. (c) Atomic-resolution spherical ACTEM image of the nanowire, clearly resolving the lattice fringes of the MoTe₂ nanowire viewed from zone axis [2 0 −4]. Upper inset: atomic configuration of the 1T′-MoTe₂ lattice viewed from the same zone axis. Lower inset: fast Fourier-transform diffractograms of the ACTEM. (d) Energy-dispersive x-ray spectroscopy (EDS) of the nanowire, revealing the sample with an atomic ratio of Te/Mo ≈ 2:1.

beam evaporation of the Ti/Au (6/60 nm) metal stacks after lift-off. The transport measurements were performed in the physical property measurement system (PPMS, Quantum Design Inc.) using the resistivity option and AC drive mode with temperature ranging from 300 to 2 K. The AC probe current $I_{AC} = 0.5\ \mu$A was applied. The device fabrication and electrical measurements were finished within 24 h to allow a more reliable data.

3. Results and discussion

The growth process of 1T′-MoTe₂ nanowires on a 280 nm SiO₂/Si substrate by CVD method is schematically shown in figure 1(a). In previous studies, the mixture of MoO₃ and NaCl powder was used as the Mo source precursor to synthesize the 1T′-MoTe₂ nanosheets [21–24]. Here the α-MoO₃ single crystal grown on mica substrate in step (I) shown in figure 1(a) is used as the Mo source precursor. The phase of the MoO₃ single crystal is confirmed by the optical image and Raman spectrum (see figure S1(b) in supporting information (https://stacks.iop.org/JPCM/33/185701/mmedia)). In step (II), the resulting MoO₃ crystal on mica is placed on SiO₂ substrate in a quartz tube, where tellurium block is placed upstream with H₂/Ar as carrying gas. It is found that the growth temperature is a critical factor for successful growth of MoTe₂ nanowires. When the growth temperature is lower than 560 °C, the product will be MoO₂ (figure S2(a)). While the growth temperature is higher than 660 °C, the product

polymer. Finally, the polymer mediator was removed by soaking in deionized water at 70–80 °C for ∼20 min. ACTEM of suspended MoTe₂ nanowire was performed with a JEM ARM 200F operated at 200 kV. SAED characterization was performed using a JEM-2100F, JEOL, operating at 120 kV and equipped with an EDS system.

2.3. Device fabrication and electrical measurements

In the material grown equipment, the end of the quartz tube was attached with the glove box with argon. The as-grown 1T′-MoTe₂ nanowires on SiO₂/Si substrate was transferred to the glove box, followed by coating poly (methyl methacrylate) (PMMA950, A5) film within argon-filled at 2000 rpm for 60 s and being baked under 60 °C for 120 s. Then, the contact metal electrodes was fabricated by using standard electron beam lithography technique (Raith 150) followed by electron
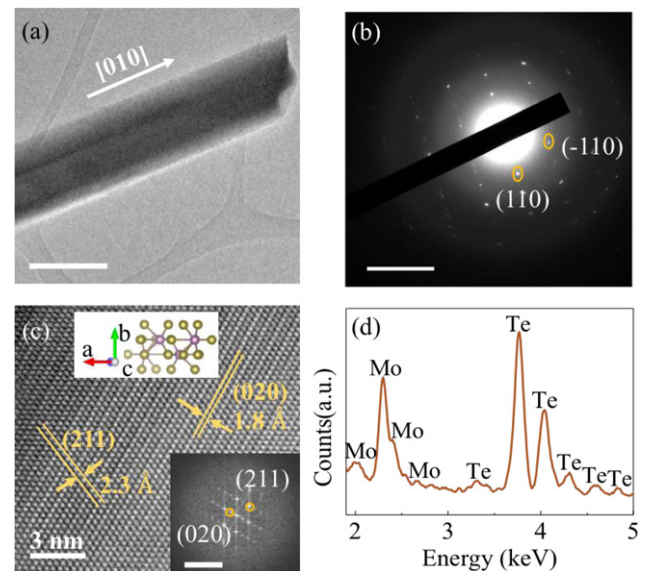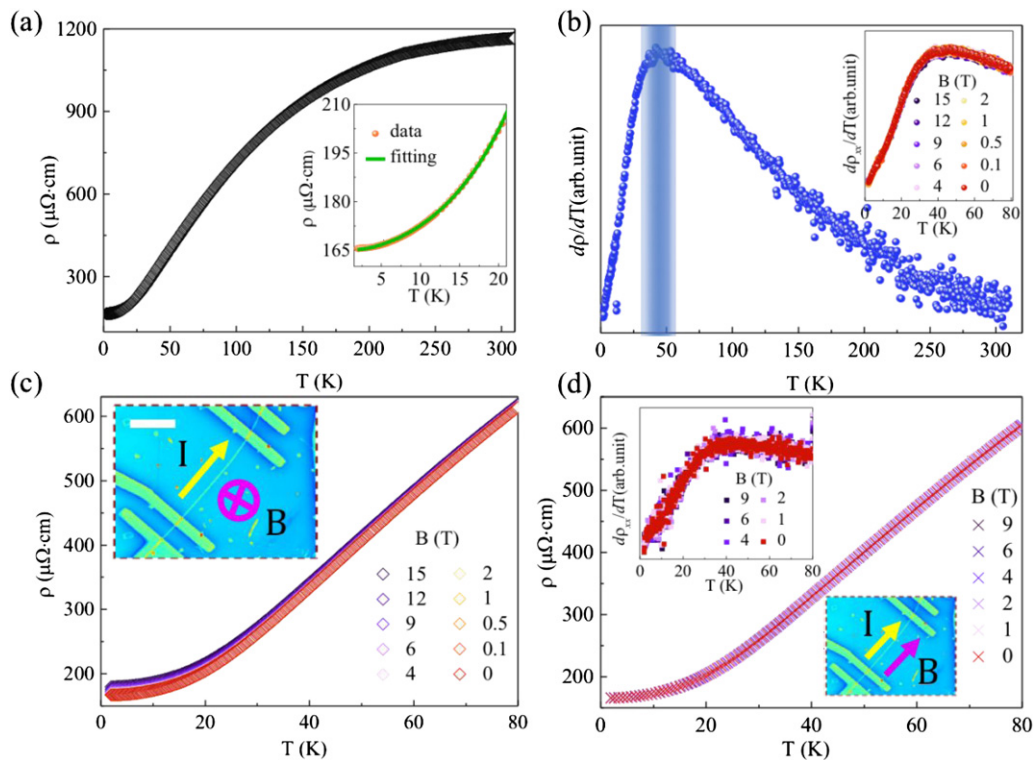
Figure 3. Temperature-dependent resistivity of MoTe$_2$ nanowire. (a) Temperature-dependent resistivity of MoTe$_2$ nanowire at zero magnetic-field. Inset, Fermi liquid and electron–phonon scattering mechanism fitting: $\rho_{xx}(T) = \rho_0 + aT^2 + bT^5$. (b) d$\rho$/d$T$ as a function of temperature for the temperature-dependent resistivity shown in (a). Inset, the temperature-dependent dρ/dT at different magnetic. (c) The temperature-dependent resistivity of MoTe$_2$ nanowire under different magnetic fields applied perpendicularly to the electrical current. Inset, the false-colored optical image of the device of MoTe$_2$ nanowire with a diameter of 31 nm. Scale bar is 5 μm. (d) The temperature-dependent resistivity of MoTe$_2$ nanowire under different magnetic fields applied parallel to the electrical current. Upper inset, the temperature-dependent dρ/dT at different magnetic fields.

will be 1T′-MoTe$_2$ nanosheets (figure S2(b)). The MoO$_2$ and 1T′-MoTe$_2$ nanosheets were identified by Raman spectroscopy (figures S2(c) and (d)). Figure 1(b) shows the typical optical image of the as-grown 1T′-MoTe$_2$ nanowires with a few tens of micrometers in length on a 280 nm SiO$_2$/Si substrate, which is grown under 580 °C with 100 sccm Ar/H$_2$ as carrier gas. The right inset of figure 1(b) shows the AFM topographic image of one typical MoTe$_2$ nanowire. The height profile (the blue curve) indicates that the diameter of the nanowire is about 41 nm. The diameter of 1T′-MoTe$_2$ nanowires is modulated from ∼27 nm–∼80 nm by simply adjusting the flow rate of carrier gas in the range from 50 to 300 sccm under a constant growth temperature (580 °C for SiO$_2$ substrate). As shown in figure 1(c), the average diameter of the MoTe$_2$ nanowires is monotonically increased with increasing Ar/H$_2$ flow rate. The diameter of 1T′-MoTe$_2$ nanowires can also be roughly identified by its color on SiO$_2$/Si substrate. In the inset of figure 1(c), the narrower 1T′-MoTe$_2$ nanowires (∼27 nm) show dark purple color, while wider nanowires (∼80 nm) show apparently shiny metallic luster. The crystal quality of 1T′-MoTe$_2$ nanowires were firstly confirmed by Raman spectroscopy with an excitation wavelength of 532 nm using a customized Raman spectrometer. Figure 1(d) shows three prominent peaks at 105, 127, and 161 cm^{-1}, respectively, which are assigned to the Raman-active A$_u$, A$_g$, and B$_g$ modes in 1T′-MoTe$_2$ [23, 25]. The inset of figure 1(d) shows the Raman

intensity mapping of peak 161 cm^{-1} of MoTe$_2$ nanowires. The homogeneous intensity across the whole region of the Raman mapping spectroscopy indicates low defect concentration in the as-grown MoTe$_2$ nanowires. For epitaxial growth of 1T′-MoTe$_2$ nanowires, fluorophlogopite mica (KMg$_3$AlSi$_3$O$_{10}$F$_2$) possessing the same symmetry (monoclinic) with 1T′-MoTe$_2$ were used as the growth substrate. Figure 1(e) shows the optical image of 1T′-MoTe$_2$ nanowires on mica (001) surface under the same growth condition with that of SiO$_2$ substrate. The 1T′-MoTe$_2$ nanowires mainly grow along three directions with respect to the edge of mica substrate and forms an angle of 60° between each other, as indicated by the yellow dashed line, suggesting an epitaxial growth mechanism [26–29].

The crystalline microstructure of the 1T′-MoTe$_2$ nanowires are further characterized by TEM. Figure 2(a) is the low-magnification TEM image of a typical MoTe$_2$ nanowire with the growth direction along [010]. Figure 2(b) is the SAED pattern of the MoTe$_2$ nanowire in figure 2(a), which is viewed from zone axis [0 0 −2]. The diffraction spots are indexed to the (−110) and (110) planes of the monoclinic 1T′-MoTe$_2$, revealing the 1T′ phase of MoTe$_2$ nanowires [23]. Figure 2(c) shows the ACTEM image of the nanowire, clearly resolving the lattice fringes of the 1T′-MoTe$_2$ nanowire. To identify the different atomic planes, fast-Fourier transformation is performed on the ACTEM image. Diffraction spots originate from the lattice planes of (020) and (211) are labeled with a zone
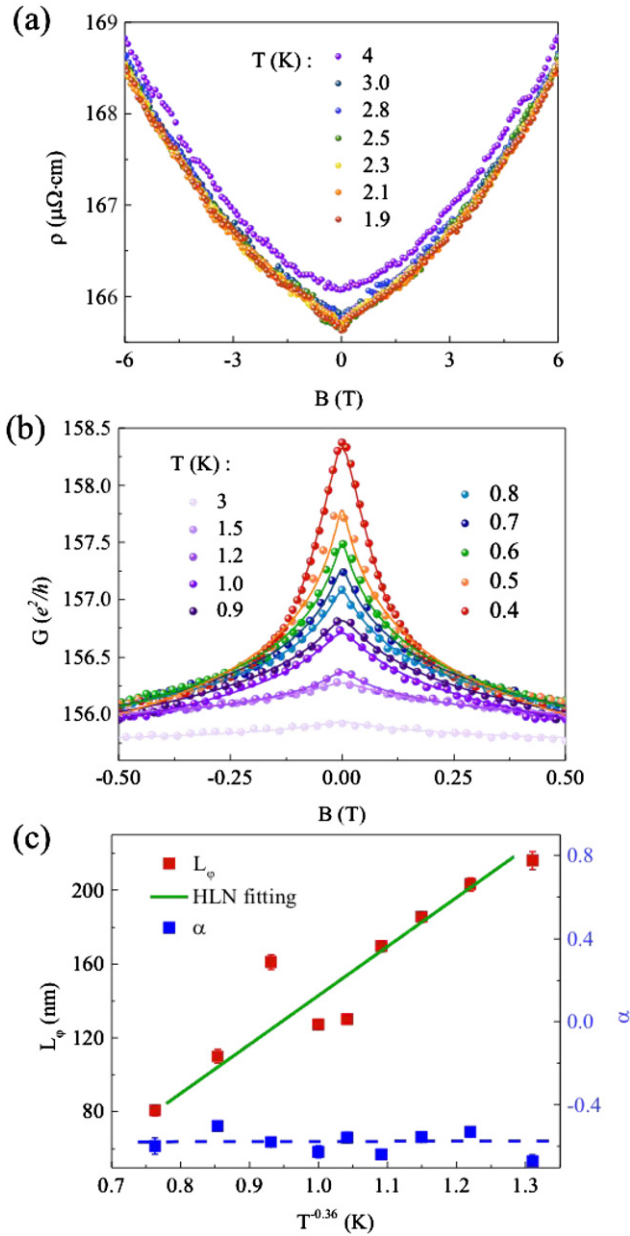
Figure 4. WAL effect in the MoTe$_2$ nanowire. (a) Magneto-resistivity of MoTe$_2$ nanowire at different temperatures. (b) HLN fitting of MR at different temperatures. Circled scatters are the experimental results and solid curves are the fitting results. (c) Phase-coherence length as a function of temperature, revealing a power-law dependence of $\sim T^{-0.36}$, consistent with the HLN model when the electrons move quasi-one-dimensionally. The pre-factor α is close to -0.5, consistent with the WAL induced by the strong SOC interaction.

axis of [2 0 −4], as shown in the lower inset in figure 2(c). The interplanar crystal spacing of (020) and (211) planes in the nanowire is measured to be 1.8 Å and 2.3 Å, respectively. This matches with the crystallographic parameters of 1T′ phase of MoTe$_2$ (ICSD#: 14 349, Space group: P2$_1$/m, $a = 6.366\,19$ Å, $b = 3.486\,88$ Å, $c = 15.547\,92$ Å, $\alpha = \gamma = 90°$, $\beta = 92.3879°$). Upper set in figure 2(c) shows the atomic configuration of the 1T′-MoTe$_2$ lattice viewed along [2 0 −4]. Furthermore, the elemental composition in the CVD-grown nanowire is examined

by the EDS, as shown in figure 2(d). There are no other impurity elements are detected except Te and Mo in the sample with the atomic ratio of Te/Mo = 20/11 = 1.82, which is very close to the stoichiometric ratio in MoTe$_2$. The smaller atomic ratio may be due to the formation of vacancy of the Te atoms during growth.

Four-probe dc resistivity measurement was carried out to characterize the electrical transport properties of the 1T′-MoTe$_2$ nanowires in a PPMS using constant current ($\sim 0.5\ \mu$A) mode. The resistivity of a typical MoTe$_2$ nanowire at zero magnetic field with temperature ranging from 2 to 300 K is shown in figure 3(a), revealing a metallic behavior in the whole temperature range. The resistivity of MoTe$_2$ nanowire at the temperatures ranging from 2 to 20 K is shown in the inset of the figure 3(a), which can be well fitted by the following equation: [30]

$$\rho(T) = \rho_0 + aT^2 + bT^5,\tag{1}$$

where ρ_0 is the residual resistivity, T^2 term stands for the Fermi-liquid contribution, T^5 term comes from the contribution of electron–phonon scattering, a and b are fitting parameters. The residual resistivity ρ_0, a, and b are listed in table S1. Moreover, the $\rho(T)$ curve shows abnormal behavior around $\sim$40 K where the d$\rho_{xx}(T)$/dT curve shows a peak near this temperature (as shown in figure 3(b)), which is probably induced by the Fermi surface reconstruction [16]. The behavior of the temperature-dependent resistivity at zero magnetic-field of 1T′-MoTe$_2$ nanowires is consistent with the bulk crystal, in which, the ratio of electron and holes concentration changes significantly around $T \sim 40$ K for the fermi surface reconstruction producing a peak in d$\rho_{xx}(T)$/dT curve at that temperature [16, 31]. In the inset of figure 3(b), the temperature-dependent dρ/dT at different magnetic fields keeps almost the same indicating that the electron structure may not be sensitive to the applied vertical magnetic fields at low temperatures. Figure 3(c) shows the temperature-dependent resistivity of 1T′-MoTe$_2$ nanowires at different vertical magnetic fields from 0 to 12 T, where no apparent changes are observed. While in the bulk crystal, the resistivity increases dramatically when temperature is lower than a certain value at higher magnetic field which is induced by the balanced hole and electron densities [30–32]. The absence of increment in resistivity under vertical magnetic fields for 1T′-MoTe$_2$ nanowires is probably induced by the heavily n-doping resulting from the Te vacancies which makes it difficult to form a balance in the hole and electron densities. To confirm this, we measured the temperature-dependent resistivity of MoTe$_2$ nanowire under different magnetic fields applied parallel to the electrical current. As shown in figure 3(d), no apparent change occurs. The absence of negative MR which is predicted in the Weyl semimetal suggests that the Fermi energy of the 1T′-MoTe$_2$ nanowires is located far above the Weyl point induced by the heavily n-doping.

Figure 4(a) shows the magnetic-field-dependent resistivity at different temperatures. The cusp feature at around zero magnetic fields at low temperatures ($<$3 K) originating from the WAL effect is observed [33–35], which becomes more

remarkable with decreasing temperatures. The temperature-dependent MR (calculated by $MR = (\rho(B) - \rho(0))/\rho(0) \times 100\%$) of additional three devices with different diameter is shown in figure S3. The cusp feature at around zero magnetic fields, as a hallmark of WAL effect, has been found in all three MoTe$_2$ nanowires. The MR of as-grown 1T′-MoTe$_2$ nanowires is suppressed in smaller diameter nanowire, where MR is close to $\sim$1.75% in 31 nm, $\sim$2.45% in 58 nm, and $\sim$4.3% in 72 nm (measured at 2 K and 6 T), respectively. This may be caused by the decrease in carrier mobility or the increase in electron–hole imbalance [20].

The WAL phenomenon shown in figure 4(a) agrees well with the one-dimension Hikami–Larkin–Nagaoka (HLN) model with strong SOC [36–39]. In the HLN model, the conductance correction $\delta G_{\mathrm{WAL}}(B)$ is given by

$$\delta G_{\mathrm{WAL}}(B) \equiv G(B) - G(0)$$
$$= \alpha \frac{e^2}{2\pi^2 \hbar} \left[\psi\left(\frac{1}{2} + \frac{B_\phi}{B}\right) - \ln\left(\frac{B_\phi}{B}\right) \right], \quad (2)$$

where B is the magnetic-field, $G(B)$ is the conductance as a function of B, ψ is the digamma function, $B_\phi = \hbar/4el_\phi^2$ with l_ϕ represents the coherence length. In the regime of strong SOC interaction [33], the pre-factor α is equal to -0.5.

As shown in figure 4(b), the MR of the 1T′ MoTe$_2$ nanowire at the magnetic fields ranging from -0.5 T to 0.5 T can be well fitted by the one-dimension HLN model. The pre-factor α is ranging from -0.50 to -0.64, which is very close to -0.5, indicating the presence of strong SOC interaction in 1T′ MoTe$_2$ nanowires. The phase-coherence length (l_ϕ) at different temperatures can be extracted and is shown in figure 4(c). Theoretically, the coherence length is proportional to $T^{-1/2}$ for the two-dimensional system and $T^{-1/3}$ for the one-dimensional system [33]. Figure 4(c) shows that the coherence length is proportional to $T^{-0.36}$, which is consistent the one-dimensional Nyquist electron–electron interaction dephasing mechanism. The present data obtained in the transport measurement affirms that the SOC play a critical role in the electronic transport properties of 1T′ MoTe$_2$ nanowires. The signature of strong SOC results in WAL effect in the metallic state can be associated with either bulk or topological surface states [40, 41].

4. Conclusions

We have developed a CVD method to prepare high-quality MoTe$_2$ nanowires by using MoO$_3$ single crystal as precursor. The WAL effect in 1T′-MoTe$_2$ nanowires caused by the strong SOC is confirmed by the low-temperature magneto-transport measurement. The diameter of the nanowires can be controlled by changing the flux of H$_2$/Ar carrier gas. An epitaxial growth can be realized by using mica (001) as the substrate. Raman spectroscopy, ACTEM and SAED characterization on the 1T′-MoTe$_2$ nanowires reveal the 1T′ phase high-quality crystallinity of the nanowires, and EDS confirms the atomic ratio of Te/Mo is close to 2:1. In temperature-dependent transport measurement, MoTe$_2$ nanowires show a metallic behavior from 2 K to 300 K, and the low-temperature

resistivity ($<$20 K) agrees well with the Fermi liquid theory with electron–phonon interaction as the main scattering mechanism. The cusp feature in MR at around zero magnetic fields at low temperatures ($<$3 K) originated from the WAL effect is observed. Based on the one dimension HLN model with strong SOC, the coherence length has been derived and is proportional to $T^{-0.36}$, indicating a Nyquist electron–electron interaction dephasing mechanism at one dimension. The availability of high-quality 1T′-MoTe$_2$ nanowires set a stage for further explorations of 1D 1T′-MoTe$_2$, provide a feasible way to prepare other one-dimensional topological materials and promise for fundamental study of the transport properties of one dimension topological materials.

Data availability

All data that support the findings of this study are included within the article (and any supplementary information files)

ORCID iDs

Jiancui Chen ⬤ https://orcid.org/0000-0003-1035-7508
Lihong Bao ⬤ https://orcid.org/0000-0002-2942-892x
Hong-Jun Gao ⬤ https://orcid.org/0000-0002-2088-0522

References

[1] Oriol L-S, Dominik L, Metin K, Aleksandra R and Andras K 2013 *Nat. Nanotechnol.* **8** 497
[2] Liu H *et al* 2019 *Nano Lett.* **19** 4551
[3] Iaia D, Chang G, Chang T-R, Hu J, Mao Z, Lin H, Yan S and Madhavan V 2018 *npj Quantum Mater.* **3** 1
[4] Yan M *et al* 2017 *Nat. Commun.* **8** 1
[5] Wang Z, Wieder B J, Li J, Yan B and Bernevig B A 2019 *Phys. Rev. Lett.* **123** 186401
[6] Tang S *et al* 2017 *Nat. Phys.* **13** 683
[7] Sanfeng W, Valla F, Quinn D G, Kenji W, Takashi T, Robert J C and Pablo J-H 2018 *Science* **359** 76
[8] Zhang Y *et al* 2010 *Nat. Phys.* **6** 584
[9] Manzeli S, Ovchinnikov D, Pasquier D, Yazyev O V and Kis A 2017 *Nat. Rev. Mater.* **2** 17033
[10] Cui J *et al* 2019 *Nat. Commun.* **10** 2044
[11] Keum D H *et al* 2015 *Nat. Phys.* **11** 482
[12] Cho S *et al* 2015 *Science* **349** 625
[13] Kappera R, Voiry D, Yalcin S E, Branch B, Gupta G, Mohite A D and Chhowalla M 2014 *Nat. Mater.* **13** 1128
[14] Song S, Keum D H, Cho S, Perello D, Kim Y and Lee Y H 2016 *Nano Lett.* **16** 188
[15] Deng K *et al* 2016 *Nat. Phys.* **12** 1105

[16] Chen F C *et al* 2018 *Phys. Rev.* B **98** 041114
[17] Yuan S, Luo X, Chan H L, Xiao C, Dai Y, Xie M and Hao J 2019 *Nat. Commun.* **10** 1775
[18] Qian X, Liu J, Fu L and Li J 2014 *Science* **346** 1344
[19] He R *et al* 2018 *Phys. Rev.* B **97** 041410
[20] Zhong S, Tiwari A, Nichols G, Chen F, Luo X, Sun Y and Tsen A W 2018 *Phys. Rev.* B **97** 241409
[21] Naylor C H *et al* 2016 *Nano Lett.* **16** 4297
[22] Zhou J *et al* 2017 *Adv. Mater.* **29** 1603471
[23] Sung J H *et al* 2017 *Nat. Nanotechnol.* **12** 1064
[24] Huang X, Zeng Z and Zhang H 2013 *Chem. Soc. Rev.* **42** 1934
[25] Kan M, Nam H G, Lee Y H and Sun Q 2015 *Phys. Chem. Chem. Phys.* **17** 14866
[26] Ji Q *et al* 2013 *Nano Lett.* **13** 3870
[27] Jie C, Yongping F, Leith S, Lianna D, Yuzhou Z, Shaohua S, Liejin G and Song J 2017 *Nano Lett.* **17** 460
[28] Dong L, Wang A, Li E, Wang Q, Li G, Huan Q and Gao H-J 2019 *Chin. Phys. Lett.* **36** 028102

[29] Li E *et al* 2018 *Chin. Phys.* B **27** 086804
[30] Zhou Q, Rhodes D, Zhang Q R, Tang S, Schönemann R and Balicas L 2016 *Phys. Rev.* B **94** 121101
[31] Pei Q L *et al* 2017 *Phys. Rev.* B **96** 075132
[32] Chen F C *et al* 2016 *Phys. Rev.* B **94** 235154
[33] Matsuo S *et al* 2012 *Phys. Rev.* B **85** 075440
[34] Weißhaupt D *et al* 2021 *J. Phys.: Condens. Matter* **33** 085703
[35] Hou Z *et al* 2018 *J. Phys.: Condens. Matter* **30** 085703
[36] Yafet Y 1963 *Solid State Phys.* **14** 1
[37] Hikami S, Larkin A I and Nagaoka Y 1980 *Prog. Theor. Phys.* **63** 707
[38] Elliott R J 1954 *Phys. Rev.* **96** 266
[39] Kurdak Ç, Chang A M, Chin A and Chang T Y 1992 *Phys. Rev.* B **46** 6846
[40] Kim J, Lee S, Brovman Y M, Kim M, Kim P and Lee W 2014 *Appl. Phys. Lett.* **104** 043105
[41] Hamdou B, Gooth J, Dorn A, Pippel E and Nielsch K 2013 *Appl. Phys. Lett.* **103** 193107